



27 **Abstract**

28 In this paper, we have developed the Matlab code for a weighted hybrid of particle swarm
29 optimization (PSO) and gravitational search algorithm (GSA) known as wPSOGSA, GSA, and
30 PSO algorithms to interpret one-dimensional magnetotelluric (MT) data for some corrupted and
31 non-corrupted synthetic data, as well as two examples of MT field data over different geological
32 terrains: (i) geothermal rich area, Island of Milos, Greece, and (ii) Southern Scotland due to the
33 occurrence of a significantly high electrical conductivity anomaly under crust and upper mantle
34 extending from the Midland Valley across the Southern Uplands into northern England. Even
35 though the fact that many models provide a good fit in a large predefined search space, specific
36 models do not fit well. As a result, we used a Bayesian statistical technique to construct and assess
37 the posterior probability density function (PDF) rather than picking the global model based on the
38 lowest misfit error. This is proceeded by 68.27 % confidence interval for selecting a region where
39 PDF is more prevalent to estimate the mean model which is more accurate and close to the true
40 model. For illustration, correlation matrices show a significant relationship among layer
41 parameters. The findings indicate, the wPSOGSA is less sensitive to model parameters and
42 produces well, more stable and reliable results with the least uncertainty in the model that is
43 compatible with existing borehole samples. Furthermore, the present methods resolve two
44 additional geologically significant layers, one highly conductive (less than 1.0 Ωm) and another
45 resistive (300.0 Ωm) over the Island of Milos, Greece, characterized by alluvium and volcanic
46 deposits, respectively, as corroborated by borehole stratigraphy.

47

48 **Keywords:** Magnetotelluric; Inversion; Uncertainty; wPSOGSA; Posterior; Bayesian.

49

50

51



52 1.0 Introduction

53 The magnetotelluric (MT) method is a natural source electromagnetic method that explores
54 various natural resources, namely hydrocarbon, minerals, geothermal prospects, groundwater,
55 metalliferous ores, etc. (Nabighian and Asten, 2002; Simpson and Bahr, 2005). Due to its
56 instability, non-unique solution, and algorithm sensitivity, the MT data interpretation is thought-
57 provoking. Many researchers have attempted and developed various inversion algorithms to
58 interpret, improve the model accuracy, convergence speed, stability and reduce the uncertainty of
59 the solutions (Kirkpatrick, et al., 1983; Constable et al., 1987; Rodi and Mackie, 2001; Li et al.,
60 2018; Zhang et al., 2019; Khishe and Mosavi, 2020). There are mainly two categories of the
61 inversion algorithm: first, the local optimization methods namely Conjugate gradient, Levenberg-
62 Marquardt/Ridge regression, Newton-Gauss, Steepest descent, and Occam inversion, requires
63 good initial guess (Shaw and Srivastava, 2007; Wen et al., 2019; Roy and Kumar, 2021) and
64 another is global optimization techniques (i.e., Ant colony optimization, Genetic algorithm,
65 Particle swarm optimization, Gravitational search algorithm, Simulated annealing, etc.) does not
66 require initial guess. Many researchers have carried out numerous metaheuristic optimization
67 algorithms to invert MT data (Dosso and Oldenburg, 1991; Pérez-Flores and Schultz, 2002;
68 Miecznik et al., 2003; Sen and Stoffa, 2013). These algorithms are inspired by the natural
69 phenomenon include Particle Swarm Optimization (Kennedy and Eberhart, 1995), Genetic
70 Algorithm (Whitley, 1994), Bat algorithm (Yang, 2010a), Differential Evolution (Storn and Price,
71 1997), biogeographically based Optimization (Simon, 2008), Firefly algorithm (Yang, 2010b),
72 Grey Wolves Optimizer (Mirjalili et al., 2014), Ant Colony (Colormi et al., 1991), Gravitational
73 Search Algorithm (Rashedi et al., 2009).

74 However, unique characteristics, namely exploration and exploitation, persist in global
75 optimization algorithms. For example, the PSO algorithm has a very high potential for
76 exploitation, which implies that the algorithm performs well in local search but is inferior in
77 exploration (Şenel et al., 2019). This suggests that the algorithm has a limited capacity to estimate



78 the best model in an extensive search range. Because of low exploration characteristics, it gets
79 trapped at the local minima (Mirjalili and Hashim, 2010). So, integrating the two algorithms with
80 opposite characteristics is the best way to solve the exploration and exploitation characteristics,
81 which provide better solutions than the results obtained from an individual algorithm.

82 Here, we utilized wPSOGSA, a new global optimization method that takes into account the
83 algorithm based on natural behavior seen in birds, fish, and insects known as Particle swarm
84 optimization (PSO) and gravity-based Newton's law (with high exploration capability) known as
85 Gravity search algorithm (GSA). Researchers interested in artificial intelligence and developing
86 effective optimization algorithms have been drawn to notable characteristics in such social
87 behavior. The wPSOGSA, PSO, and GSA are used to estimate resistivity distribution of a multi-
88 layered 1D earth model using synthetic (noise free and noisy) data for three and four layers cases
89 taken from Shaw and Srivastava (2007) and Xiong et al. (2018), respectively and field MT
90 sounding data for four and six layers cases taken from Jones and Hutton (1979).and Hutton et al.
91 (1989) respectively.

92 Furthermore, numerous (here 10000) models that fit well are optimized for getting the
93 mean model, which is proceeded by calculating posterior PDF based on Bayesian concepts
94 using all accepted models to find the optimal mean solution with the least uncertainty, as well
95 as a correlation matrix to determine the relationships among the layer parameters. Thus, our
96 analysis suggests that the wPSOGSA algorithm offers a more accurate and trustworthy model
97 with better stability, fast convergent rate and the least uncertainty in the model.

98

99 **2.0 Forward Modelling- Magnetotelluric formulation for 1-D earth**

100 The ability to formulate an effective inversion method requires a thorough understanding of the
101 forward modeling technique for the issue of interest. Factors like frequency range, actual
102 resistivity, and layer thickness are used to create synthetic MT apparent resistivity, $\rho_a(\omega)$ and
103 apparent phase, $\varphi_a(\omega)$ data sets. The electromagnetic impedance (Z) for layered structures is



104 described in terms of an orthogonal horizontal electric field, magnetic field, wavenumber (k),
105 reflection coefficient (R), and exponent factor (τ_f) with angular frequency (ω) as (Ward and
106 Hohmann, 1988):

$$107 \quad Z = \frac{\mu_0 \omega}{k} = \frac{E_x}{H_y} = -\frac{E_y}{H_x}, \quad (1)$$

108 Where, the wavenumber(k) = $\sqrt{-i\mu_0\omega/\rho}$, component of electric field (E_x and E_y) and magnetic
109 field component (H_x and H_y).

110 If displacement currents are not taken into account, Eq. (1) becomes

$$111 \quad Z = \frac{\mu_0 \omega}{\sqrt{-i\mu_0\omega/\rho}} = \sqrt{i\mu_0\omega\rho} = \sqrt{\mu_0\omega\rho} e^{\frac{i\pi}{4}} = \omega \frac{(1 - R \tau_f)}{(1 + R \tau_f)}, \quad (2)$$

112 Noisy impedance is calculated by the following equation

$$113 \quad Z_{noisy} = Z + Z \times (2 \times rand - 1) \times noise_{percent}, \quad (3)$$

114 If the angle between impedance phase with E_x is 45^0 , then the resistivity (ρ) in half-space of
115 impedance $Z(\omega)$ and time period (T) can be written as

$$116 \quad \rho(\omega) = \frac{1}{\mu_0 \omega} |Z(\omega)|^2 = \frac{0.2T}{\mu_0} \left| \frac{E_x}{H_y} \right|^2, \quad (4)$$

117 Thus, the apparent resistivity and apparent phase are defined (Cagniard, 1953; Ward and
118 Hohmann, 1988) as follows:

$$119 \quad \text{Apparent resistivity, } \rho_a(\omega) = \frac{1}{\mu_0 \omega} [Z(\omega)Z^*(\omega)], \quad (5)$$

$$120 \quad \text{Apparent phase, } \varphi_a(\omega) = \tan^{-1} \left(\frac{\text{img}(Z(\omega))}{\text{real}(Z(\omega))} \right), \quad (6)$$

121 Where the exponent factor, $\tau_f = \exp(-2\gamma h)$, the induction parameter $\gamma = \sqrt{i\omega\mu_0/\rho}$, h is the
122 layer thickness, μ_0 is the magnetic permeability for free space, Z^* is the complex conjugate of
123 impedance, and the *rand* is used for generating random number between 0 and +1.

124

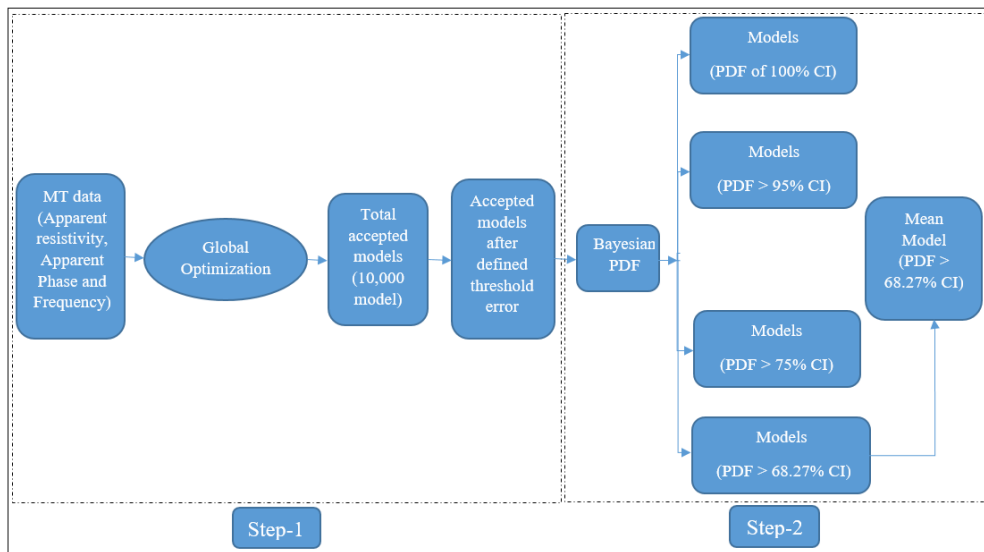
125

126



127 **3.0 Methodology**

128 The methodology that we used for joint modeling of metaheuristic global optimization namely
129 PSO, GSA, and wPSOGSA in Step-1 and posterior Bayesian probability density function
130 technique in Step-2 to obtain the global model by utilizing the synthetic and field MT apparent
131 resistivity and phase curves is depicted in the schematic diagram (Fig. 1), and the steps are
132 described below:



133
134 **Figure 1** Schematic diagram demonstrating the essential processes considered for joint modeling
135 of metaheuristic global optimization (Step-1) and posterior PDF technique (Step-2) for obtaining
136 the global model by utilizing the synthetic and field MT data

137

138 **3.1 Optimization and Error Estimation**

139 In the present study, we have implemented a new innovative global optimization technique known
140 as wPSOGSA, in which swarm particles and mass particles provide the best particle, i.e., the best
141 model. The best model is chosen based on the fitness of the particles, and the cost function or
142 objective function is used to estimate this fitness. Thus magnetotelluric (MT) inverse problem can
143 be formulated through the forward modelling operator, f , aim at achieving the resistivity model,



144 which illuminates the observed data ρ in the foremost. This operator combines the problem of
145 physics and inverts the observed apparent resistivity data to the resistivity-depth model, \mathbf{x} , as

$$146 \quad (\rho, \varphi) = f(\mathbf{x}), \quad (7)$$

147 The cost function (fitness of the particle) is a mathematical relation between observed and
148 calculated data and it is defined as the root mean square error (RMS):

$$149 \quad RMS = \sqrt{\left\{ \frac{(\rho - \rho_C)^2}{N} + \frac{(\varphi - \varphi_C)^2}{N} \right\}}, \quad (8)$$

150 Where N is the total observed data points, ρ and φ are the observed apparent resistivity and phase,
151 ρ_C and φ_C are the computed apparent resistivity and phase data.

152

153 3.2 Particle swarm optimization

154 The particle swarm optimization (PSO) technique is a widespread evolutionary optimization
155 approach for determining the optimal global solution to a nonlinear inverse problem (Kennedy
156 and Eberhart, 1995). This technique is analogous to the particle's natural behavior in search of
157 food with the help of collaborative support from the model population represented by geophysical
158 resistivity solutions/models (known as particles) in a swarming group. The best model/position
159 obtained among the particles so far is stored for each iteration, which helps in search for the best
160 solution, defined by the fitness of each particle estimated using Eq. (8). The particles' velocity and
161 location in the search space are defined for k^{th} particle at t^{th} iteration is given below:

$$162 \quad v_k(t+1) = wv_k(t) + c_1 \times rand \times (x_p - x_k(t)) + c_2 \times rand \times (x_g - x_k(t)), \quad (9)$$

$$163 \quad x_k(t+1) = x_k(t) + v_k(t+1), \quad (10)$$

164 where w is the inertia weight set in between 0 and 1, c_1 and c_2 are a personal learning coefficient
165 and a global learning coefficient, respectively, $v_k(t)$ is the velocity of the k^{th} particle at t^{th} iteration,
166 and $rand$ is used for a random number between 0 and 1, x_p is the present best solution. x_g is the
167 global best solution, $x_k(t)$ is the position of the k^{th} particle at t^{th} iteration. Particles change their



168 position at each iteration to approach an optimum solution. The first, second, and third terms in
169 Eq. (9) represent exploratory ability, private thought, and particle collaboration, respectively.

170

171 3.3 Gravitational search algorithm

172 The gravitational search algorithm (GSA) is a meta-heuristic algorithm based on Newton's
173 gravitational law (Rashedi et al., 2009), which states that mass particles attract each other with a
174 gravitational force that is directly proportional to the product of their masses and inversely
175 proportional to the square of the distance between them. It signifies that massive particles (here,
176 particle represents the resistivity layer model/solution) attract to the neighboring lighter particles.
177 Similar to PSO, the Gravitational search optimizer works with a population of particles known as
178 mass particles in the universe. Thus the best model/solution/particle is achieved among the mass
179 particles. The best model is defined by each particle's capability (i.e., the fitness) calculated using
180 Eq. (8). The initialization of their position in the search spaces is given by

$$181 \quad x = rand(N, D) \times (up - down) + down, \quad (11)$$

182 Where N , D are the number of particles/models, the dimension of the model; and up , and $down$
183 are the upper and lower limit of the search range, respectively.

184 During execution time, the gravitational acting force on agent k^{th} from agent j^{th} at a specific
185 time (t) is defined as

$$186 \quad F_{k,j}(t) = G(t) \frac{M_{p,k}(t) * M_{a,j}(t)}{R_{k,j}(t) + \epsilon} (x_j(t) - x_k(t)), \quad (12)$$

187 Where, $M_{a,j}$, and $M_{p,k}$ are the active and passive gravitational masses for particle j and k ,
188 respectively, $x_j(t)$ is the position of the particle j at a time t for various parameters, $R_{k,j}(t)$ is
189 Euclidian distance between two particles, and ϵ is a small constant.

190 Here, gravitational constant $G(t)$ at a specific time t is defined as (Kunche et al., 2015)
191 and acceleration of k^{th} agent at t^{th} iteration for models is $ac_k(t)$ is defined as:

$$192 \quad ac_k(t) = \frac{F_k(t)}{M_k(t)}, \quad (13)$$



193 Where the gravitational acting force on agent k from agent j and $M_k(t)$ is the mass of the object at
194 a specific time (t).

$$195 \quad G(t) = G_0 \times \exp\left(-\alpha \times \frac{iter}{maxiter}\right), \quad (14)$$

196 Where α , G_0 , $iter$, and $maxiter$ are descending coefficients, starting value of gravitational constant,
197 current iteration, and maximum iterations, respectively.

198 The following equations are used to update the particle's velocity and location:

$$199 \quad v_k(t + 1) = rand \times v_k(t) + ac_k(t), \quad (15)$$

$$200 \quad x_k(t + 1) = x_k(t) + v_k(t + 1), \quad (16)$$

201 All the particles are randomly placed in the search range using Eq. (11) and then initializes the
202 particle's velocity. Meanwhile, the gravitational constant, total forces and acceleration are
203 computed, and the locations are updated. The end criteria is the misfit error (i.e. 10^{-9}) is taken in
204 our study.

205

206 **3.4 Weighted hybrid PSO-GSA (wPSOGSA)**

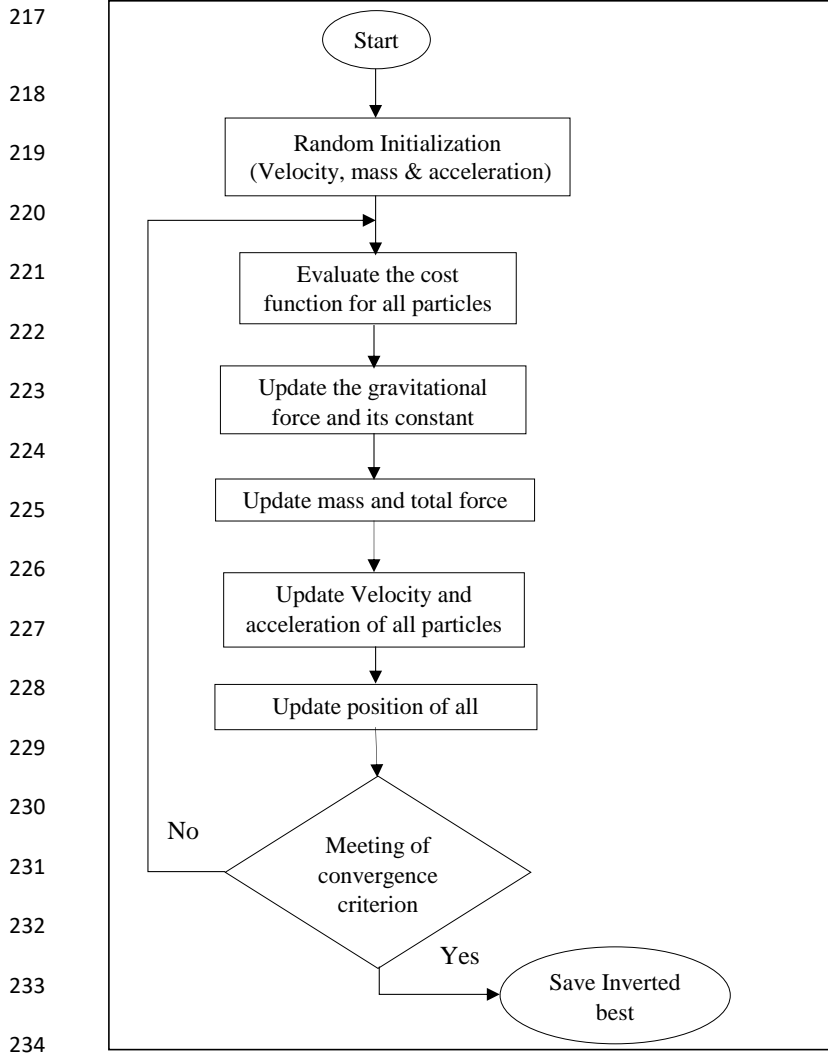
207 The weighted hybrid of PSO and GSA algorithm known as the wPSOGSA algorithm integrates
208 two essential characteristics, exploration (i.e., the ability of an algorithm to search the whole range
209 of a given parameter) and exploitation (i.e., the ability to converge the solution nearest to the best
210 solution) of the global optimization algorithm that increases its efficiency and converges the
211 objective function to achieve global minima. The velocity and location of the particles updated in
212 the wPSOGSA algorithm are illustrated in the schematic diagram (see Fig. 2).

213

214

215

216



235 **Figure 2** Flow chart of the weighted hybrid Particle Swarm Optimization and Gravity Search
 236 Algorithm known as the wPSOGSA algorithm (After (Mirjalili and Hashim, 2010))

237 The wPSOGSA combines the characteristic of social thinking of PSO and the searching
 238 capability of GSA; thus, the particle’s velocity is defined as

239
$$v_k(t + 1) = w \times v_k(t) + c_1 \times rand \times ac_k(t) + c_2 \times rand \times (x_g - x_k(t)) , \quad (17)$$

240 Where $v_k(t)$ is the velocity of the particle k at iteration t , w is the weight function (i.e., the constant
 241 which helps to control the momentum of the algorithm to perform optimization properly), $ac_k(t)$



242 is the acceleration of agent k , x_g is the best solution, and the rand is a random number lies between
243 0 and 1. At each iteration, particles updated their location to achieve the best solution defined as

$$244 \quad x_k(t+1) = x_k(t) + v_k(t+1), \quad (18)$$

245 The algorithm starts by randomly initializing the velocity, mass, and acceleration of the
246 particles. The cost function is evaluated for all particles for specified iterations to get the most
247 optimal solution, and inverted results are updated at each iteration. Equation (12), (17), and (18)
248 are used to update the gravitational force, velocity, and location of particles after initialization.
249 However, the velocity and position stop updating their values when the algorithm converge and
250 reaches the least error of the cost function.

251

252 **3.5 Bayesian probability density function**

253 In a Bayesian framework, the probability distribution of the model parameters (known as posterior
254 probability distribution) is computed using given observed data and models obtained from
255 inversion. The posterior for a model is calculated using Bayes' theorem and previous model space
256 information. Individual model parameter ranges are incorporated in the prior knowledge. The two
257 fundamental stages in the Bayesian statistics method are the representation of previous knowledge
258 as a probability density function and calculating the likelihood functional derived from data misfit
259 (Tarantola and Valette, 1982). Specific characteristics, such as the best fitting model, mean model,
260 and correlation matrix may be determined from posterior distribution of models. According to the
261 Bayes' theorem,

$$262 \quad \text{Posterior} = \text{prior} \times \text{likelihood}, \quad (19)$$

263 As a result, our priori distribution function for the parameter, x_u , mean priori information, M , and
264 t^2 is the mean uncertainty (μ) is defined as

$$265 \quad f(\mu) = \frac{1}{\sqrt{2\pi t^2}} \exp\left\{-\frac{(x_u - M)^2}{2t^2}\right\}, \quad (20)$$

266 and likelihood function is



267
$$f(X|\mu) = \prod_{u=1}^n \frac{1}{\sqrt{2\pi\sigma^2}} \exp\left\{-\frac{(x_u-\mu)^2}{2\sigma^2}\right\}, \quad (21)$$

268 Hence the posterior density function calculated for a parameter (x_u) using mean (μ) and variance
 269 (σ^2) defined (Lynch, 2007) as

270
$$f(\mu|X) = \frac{1}{\sqrt{t^2\sigma^2}} \exp\left\{\frac{-(\mu-M)^2}{2t^2} + \frac{\sum_{u=1}^n (x_u-\mu)^2}{2\sigma^2}\right\} \quad (22)$$

271 The posterior Bayesian PDF is calculated from accepted models within a set of parameters, as
 272 shown below:

273
$$P(X|E) = \frac{P(X)L(E|X)}{\sum_X P(X)L(E|X)}, \quad (23)$$

274 Where, $P(X|E)$ is the posterior probability distribution of the parameter (X) given the evidence
 275 (E), $P(X)$ is the prior information of (X) and $L(E|X)$ is the likelihood function of X.

276 After the application of PDF, the study is further proceeded by choosing Confidence
 277 Interval (CI) of 68.27 % that is based on the empirical rule, known as the 68-95-99.7 rule (Ross,
 278 2009). The model parameters below 68.27 % CI are discarded, and the remaining parameters are
 279 used for determining the mean model and uncertainty. Thus, the mean model (P_j) is calculated
 280 using the best models having PDF within a 68.27 % CI, defined in the following equation:

281
$$P_j = \exp\frac{1}{Nd} \sum \ln(P_{j,k}), \quad (24)$$

282 Here accepted models are used to calculate the correlation matrix (i.e., correlation among
 283 model parameters lie between -1 and 1) using the following equation (Tarantola, 2005):

284
$$CovP(l,j) = \frac{1}{Nd} \sum (P_{l,k} - P_l) (P_{j,k} - P_j), \quad (25)$$

285 and
$$CorP(l,j) = \frac{CovP(l,j)}{\sqrt{CovP(l,l) \times CovP(j,j)}}, \quad (26)$$

286 Here, N is the total number of models, d is used for the number of the layer parameters, $P_{j,k}$ is the
 287 j^{th} model parameter of k^{th} model where l and j both vary from 1 to d (number of layer parameters).

288 $CovP(l,j)$ is the covariance matrix between model parameter l and j , $P_{l,k}$ is the model parameter



289 l^{th} model parameter of k^{th} model and $CorP(l, j)$ is the correlation matrix between model parameter
290 l and j .

291

292 **4.0 Results and discussions**

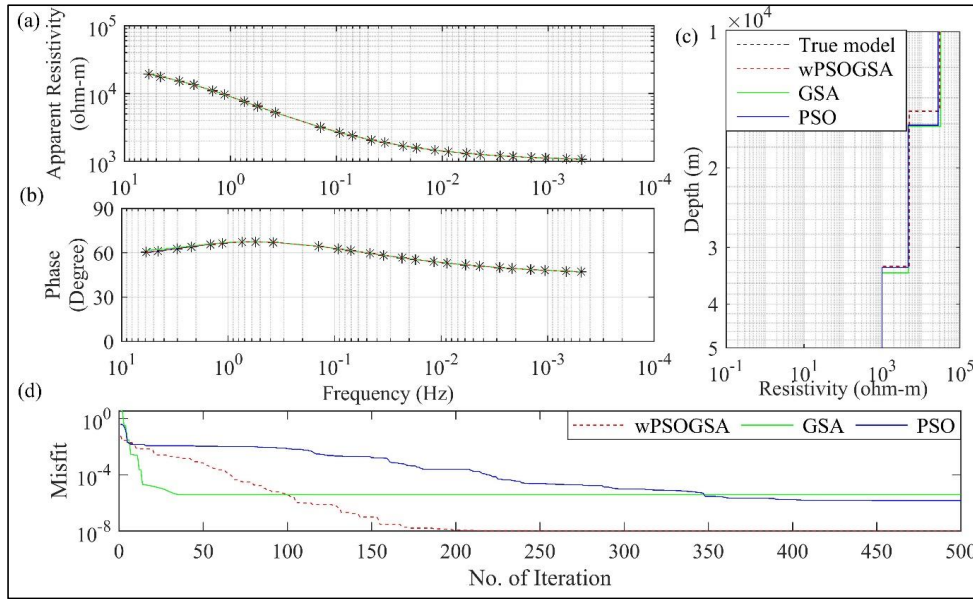
293 Different MT datasets are utilized to evaluate the proposed wPSOGSA algorithm's effectiveness,
294 sensitivity, stability, and robustness in outlining the genuine subsurface structure. These datasets
295 are noise-free and Gaussian noise synthetic data produced for several geological formations, and
296 two MT field data have been optimized for analysis.

297

298 **4.1 Application to synthetic MT data-Three layers case**

299 To demonstrate and evaluate the robustness of the present algorithms, we have generated apparent
300 resistivity and apparent phase synthetic MT data without noise and with noise levels (10 % and
301 20 % noise) considering a three-layer typical continental crustal model with a total thickness of
302 33000 m (i.e., 33.0 km) having a resistivity of middle crust 5000.0 Ωm with 18000 m (i.e., 18.0
303 km) thickness (reasonable low resistive layer) and resistivity of upper-crust 30000.0 Ωm with
304 15000 m (i.e., 15 km) thickness (high resistive layer) underlain by 1000 Ωm (low resistive) half
305 space taken from Shaw & Srivastava (2007).

306 This synthetic MT data that was executed for 10000 runs keeping the same lower and upper
307 bounds as given in Table 1, and iteration to 1000. Figure 3 shows (a) the observed apparent
308 resistivity with the computed data, (b) the observed apparent phase with the computed data, (c)
309 1D inverted model by wPSOGSA (red color), GSA (green color) and PSO (blue color) with a true
310 model (black color), and 2(d) shows the relation between misfit and iterations for the noise-free
311 synthetic data.



312

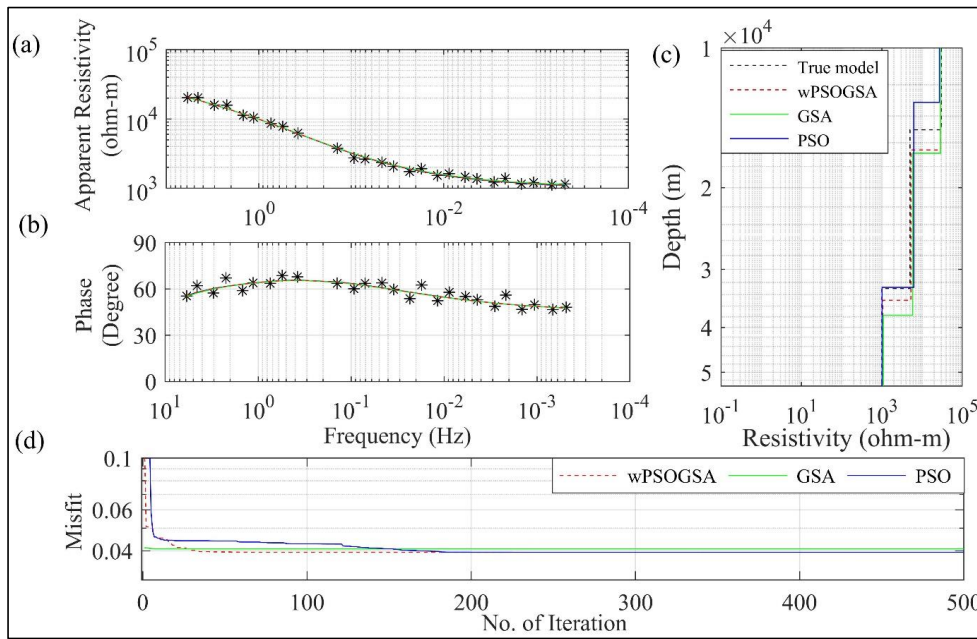
313 **Figure 3** The inverted MT response by PSO (blue color), GSA (green color), and hybrid
 314 wPSOGSA (red color) with a true model (black color) over three-layer synthetic data as shown in
 315 (a) observed and calculated apparent resistivity curve, (b) observed and calculated apparent phase
 316 curve, (c) 1D depth inverted model, and (d) misfit error versus iterations

317 The misfit curve as shown in Fig. 3(d) is gradually decreasing with increasing iterations
 318 and becomes constant, where the algorithm converges. The PSO, GSA, and wPSOGSA converge
 319 at iterations 492, 35, and 316 with associated errors $1.51e-6$, $3.97e-6$, and $1.035e-8$, and the
 320 associated computational time is 27.06 seconds, 1.75 seconds, and 3.35 seconds, respectively.
 321 Thus the curves describes that wPSOGSA converges at the least RMS error. Whereas PSO, GSA,
 322 and wPSOGSA using 10 % noisy synthetic data converge at 102, 88, and 358 iterations with an
 323 associated error are 0.00435, 0.00439, and 0.00426, and associated computational times are 5.61
 324 seconds, 4.40 seconds, and 3.80 seconds, respectively.

325 Figure 4 presents the 20 % noisy synthetic MT data that was executed for 10000 runs
 326 keeping the same lower and upper bounds, and iteration to 1000. The well fitted inverted MT
 327 response (see Fig. 4) as follows: (a) the corrupted synthetic and calculated apparent resistivity



328 data, (b) the corrupted synthetic and calculated apparent phase data, (c) the inverted 1D depth
329 model, and (d) convergence response in terms of misfit error versus iterations. We analyzed Fig.
330 4(d) and found that the PSO, GSA, and wPSOGSA using noisy synthetic data converge at
331 iterations 236, 7, and 73 with associated errors 0.0394, 0.0408, and 0.0393, respectively.
332



333
334 **Figure 4** The inverted MT response by PSO (blue color), GSA (green color), and hybrid
335 wPSOGSA (red color) with a true model (black color) over three-layer synthetic data with 20 %
336 random noise as shown in (a) observed and calculated apparent resistivity curve, (b) observed and
337 calculated apparent phase curve, (c) 1D depth inverted model, and (d) misfit error versus iterations

338

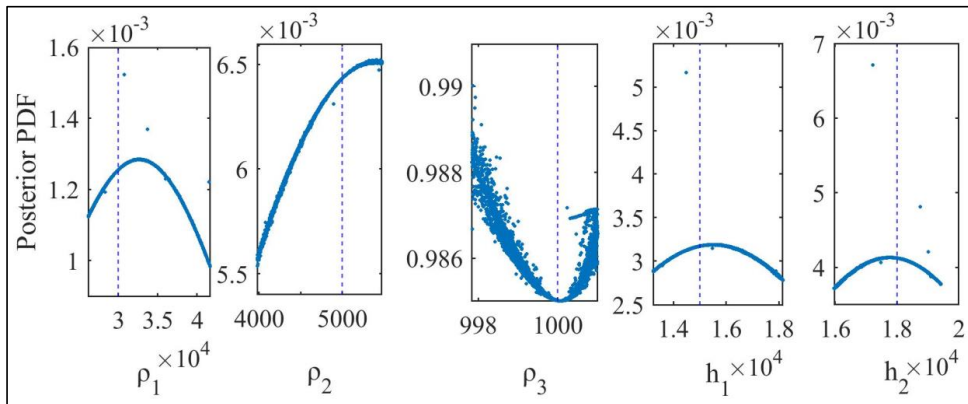
339 4.1.1 Bayesian analysis and uncertainty in model parameters

340 Two methods are used to estimate mean solution and uncertainty: one method is the mean solution
341 for all accepted best-fitted solutions acquired from 10,000 runs for all three global optimization
342 techniques; another method is the model derived from all approved solutions using posterior



343 Bayesian PDF within one standard deviation. To get the global best solutions in our study, we
 344 incorporated posterior PDF based on the Bayesian approach to enhance the efficacy of the inverted
 345 model and minimize the uncertainty in the model. The process for obtaining the mean solution is
 346 proceeded by selecting an initial threshold error which is essential because the smaller the
 347 threshold value, the more significant number of models with lesser uncertainty in the model
 348 parameters (Sharma, 2012). Thus, a more considerable threshold gives a lesser number of models
 349 with enormous uncertainty in the model parameter (Sen and Stoffa, 1996; Sharma, 2012). This is
 350 further proceeded by calculating the PDF for each parameter value using Eq. (22). In order to
 351 select values of each parameter that having higher posterior PDF, a 68.27 % CI is used. The mean
 352 model obtained from selected model parameters is near to the actual model.

353 Figure 5 shows the output of posterior Bayesian PDF, which select model parameters
 354 with lesser error. The straight lines (dashed lines) present the actual value of the respective layer
 355 parameters. The first layer thickness, second layer thickness, and first layer resistivity have
 356 higher uncertainties, i.e., 61.25 m, 51.47 m, and 210.61 Ωm , respectively, whereas the second
 357 layer resistivity and third layer resistivity have lower uncertainty, i.e., 17.71 Ωm and 0.03 Ωm ,
 358 respectively.



359
 360 **Figure 5** Posterior Bayesian probability density function (PDF) with 68.27 % CI for wPSOGSA
 361 for three-layered synthetic data



362 **Table 1** True model, search range, and inverted layer parameters by hybrid wPSOGSA, GSA, and
 363 PSO for three-layer with different noise (0 %, 10 %, and 20 %) synthetic MT apparent resistivity
 364 and apparent phase data.

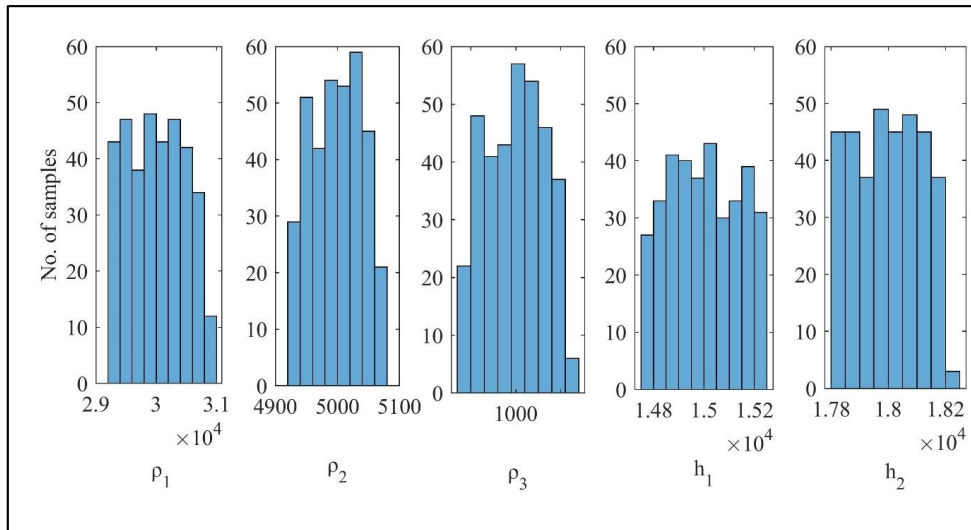
Layer parameters		ρ_1 (Ωm)	ρ_2 (Ωm)	ρ_3 (Ωm)	h_1 (m)	h_2 (m)
True model		30000	5000	1000	15000	18000
Search Range		5000 - 50000	1000 - 10000	50 - 5000	5000 - 25000	10000- 25000
(Shaw & Srivastava, 2007) 2.0 % Gaussian random noise	PSO	26981.80	6230.30	1011.70	13090	19720
	GA	40800	10000	1010	6210	25000
	RR	43424.40	3097.10	980.70	17010.00	16960.00
0 % noisy data	PSO	27463.86	4664.57	999.48	16112.66	17080.01
	GSA	32017.78	4721.69	1004.05	16195.26	17928.07
	wPSOGSA	30243.42	5007.04	1000.02	14969.33	18029.76
10 % noisy data	PSO	19861.54	7659.73	1022.19	15971.66	14774.31
	GSA	27538.91	6534.61	1018.04	14117.82	17408.14
	wPSOGSA	27589.85	6043.87	998.99	14902.89	18221.87
20 % noisy data	PSO	26981.8	6230.3	1011.7	13090.00	19720.00
	GSA	28823.57	5825.19	1089.65	16861.84	20795.48
	wPSOGSA	29208.75	5282.77	1055.09	16573.22	18398.94

365

366 Table 1 shows the inverted layer parameters using wPSOGSA, GSA, and PSO for noise-
 367 free and noisy synthetic MT databased on posterior Bayesian PDF, as well as the actual model and
 368 the search range. In addition, layered properties of synthetic data corrupted with 10 % and 20 %
 369 random noise are compared and statistically analyzed. Our findings, as shown in Table 1, were
 370 compared to those obtained using the Genetic Algorithm (GA), Ridge Regression (RR), and PSO



371 by Shaw & Srivastava (2007), which consistently outperforms GA and RR is closer to the genuine
372 model.



373

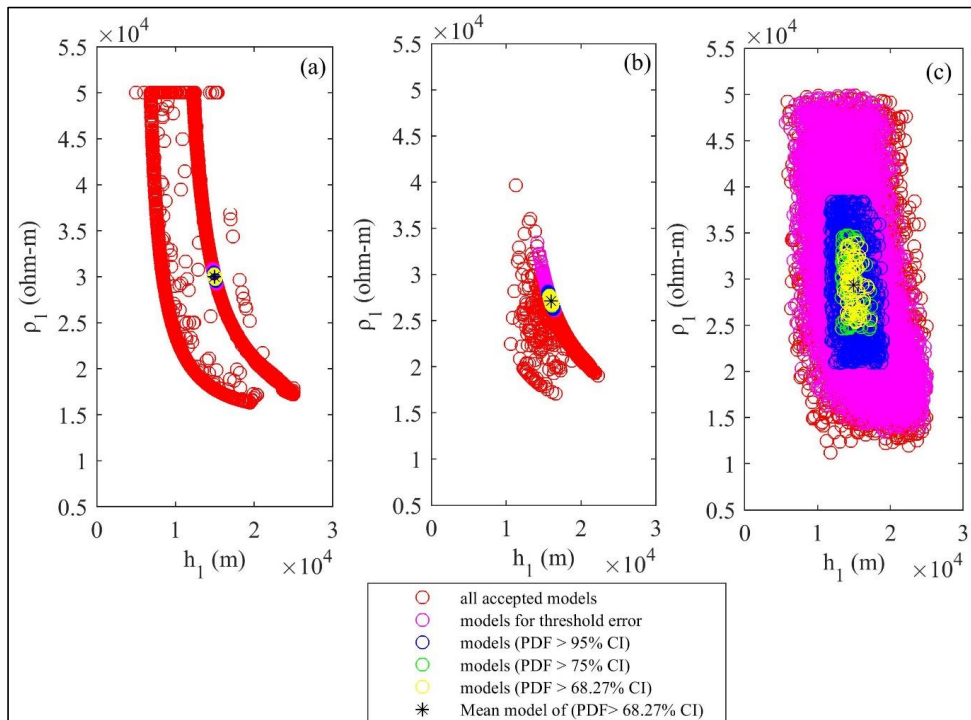
374 **Figure 6** Histogram of selected models for misfit error below a defined threshold error of
375 wPSOGSA

376 Mean value of the accepted model parameters (30243.42 ± 471.26 , 5007.04 ± 39.59 ,
377 1000.02 ± 0.064 , 14969.33 ± 136.82 , 18029.76 ± 114.90) with high uncertainty of the parameters (1.5
378 %, 0.78 %, 0.0064 %, 0.91 %, and 0.63 %). On the basis of low posterior PDF and high
379 uncertainty, we have taken (ρ_1) and (h_1) for the exercise to show the models are not biased to the
380 selected models.

381 As well as based on the histograms (see Fig. 6), posterior PDF and uncertainty of the
382 inverted layer parameters resistivity (ρ_1) and thickness (h_1) for the three-layered synthetic MT data
383 have been taken to depict the global solution using presented algorithm. Here we prepared the
384 cross-plots of ρ_1 versus h_1 using (a) wPSOGSA, (b) PSO, and (c) GSA, showing all accepted
385 models (red circle), selected models with misfit error less than a threshold error of 10^{-4} (magenta
386 circle), models of a PDF greater than 95 % (blue circle), models of a PDF greater than 75 % (green



387 circle), models of a PDF greater than 68.27 % (yellow circle), and mean model, i.e., model
 388 parameters which having a PDF greater than 68.27 % (black asterisk) as shown in Fig. 7. It is
 389 noticed that the all inverted results give the global solution which has a good agreement with the
 390 true model, whereas wPSOGSA gives the more accurate results than the other two algorithms PSO
 391 and GSA as shown in Table 2.



392 **Figure 7** Cross-plots of thickness and resistivity of first layer for the three-layered synthetic
 393 resistivity model using (a) wPSOGSA, (b) PSO, and (c) GSA, displaying all accepted models (red
 394 circle), selected models with misfit error less than a threshold error (magenta circle), models (pdf
 395 > 95 % CI, blue circle), models (pdf > 75 % CI, green circle), models (pdf > 68.27 % CI, yellow
 396 circle), and mean model i.e. model parameters which having a PDF greater than 68.27 % (black
 397 asterisk)

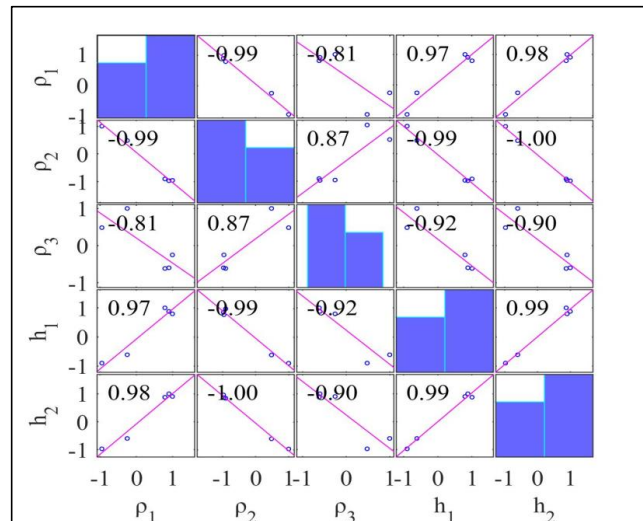
399



400 **4.1.2 Sensitivity, correlation matrix, and model parameters**

401 The accepted models, which have posterior PDF value within 68.27 % CI, are used to calculate
 402 the correlation matrix. This correlation matrix gives the relationship among model parameters.
 403 Thus, the lesser correlation value gives weak relation among the parameters and vice versa. The
 404 correlation matrix of PSO, GSA, and wPSOGSA was examined on one set of synthetic data, as
 405 shown in Fig. 8, Fig. 9 and Fig. 10, demonstrating the sensitivity among inverted model
 406 parameters. The value of correlation matrix 1.0 indicates that the two parameters are strongly
 407 correlated.

408 Figure 8 shows that first layer resistivity is correlated highly positively with a first-layer
 409 thickness (0.97) and second layer thickness (0.98), while the second layer resistivity (-0.99) and
 410 third layer resistivity (-0.81) are substantially negative connected. Second layer resistivity is
 411 correlated with the third layer resistivity (0.87) which has a significant positive relationship; while
 412 second layer resistivity has a significant negative correlation with the first layer thickness (-0.99)
 413 and the second layer thickness (-1.00). First layer thickness (-0.92) and second layer thickness (-
 414 0.90) are very negatively associated with third layer resistivity, while first layer thickness is
 415 extremely positively correlated with a second layer thickness (0.99).



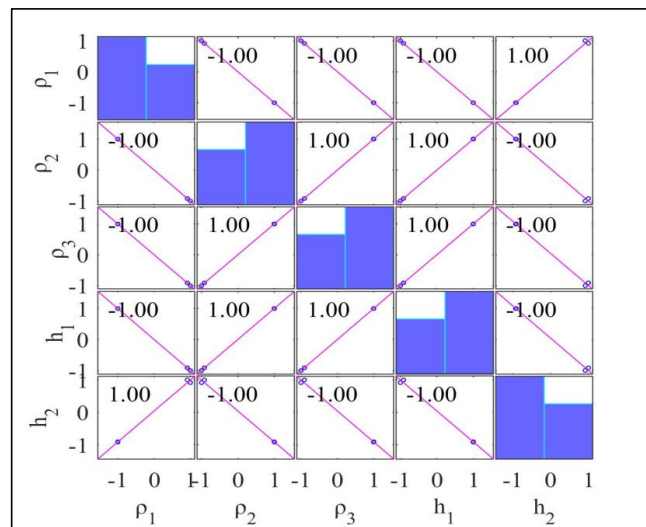
416



417 **Figure 8** Correlation matrix calculated from PSO inverted model using a three-layer noise-free
 418 synthetic MT apparent resistivity and apparent phase data

419

420 Figure 9 indicates that first layer resistivity is highly associated with a second layer
 421 thickness (1.00) and weakly with second layer resistivity (-1.00), third layer resistivity (-1.00),
 422 and first layer thickness (-1.00). Second layer resistivity (-1) is highly linked with a second layer
 423 thickness (-1.00), while third layer resistivity (1.00) and first layer thickness are strongly
 424 correlated (1.00). Third layer resistivity has a highly positive correlation with a first-layer
 425 thickness (1.00) and a strong negative correlation with a second layer thickness (-1.00), whereas
 426 first layer thickness has a significant negative correlation with a second layer thickness (-1.00).



427

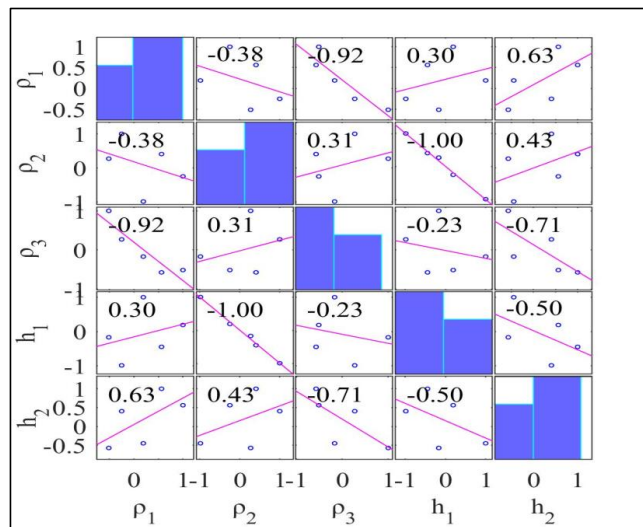
428 **Figure 9** Correlation matrix calculated from GSA inverted model using a three-layer noise-free
 429 synthetic MT apparent resistivity and apparent phase data

430

431 Figure 10 shows the correlation matrix of wPSOGSA. The analyses reveal that the first
 432 layer resistivity is strongly negative with the second layer resistivity, substantially negative (-0.92)
 433 with the third layer resistivity, weakly positive (0.30) with the first layer thickness, and



434 considerably (0.63) with the second layer thickness. Second layer resistivity is slightly positive
 435 (0.31) when compared to third layer resistivity (0.43) but substantially negative when compared
 436 to first layer thickness. Third layer resistivity has a slightly negative correlation (-0.23) with first
 437 layer thickness, but a moderately negative correlation (-0.71) with second layer thickness and first
 438 layer thickness has a negative correlation (-0.71). Thus the conclusion can be made that the layer
 439 parameters are independent of others, so changing one will have no effect on the other compared
 440 to the result obtained via PSO and GSA algorithms.



441

442 **Figure 10** Correlation matrix calculated from wPSOGSA inverted model using a three-layer
 443 noise-free synthetic MT apparent resistivity and apparent phase data

444

445 4.1.3 Stability analysis

446 We used two different search ranges for stability evaluation of proposed wPSOGSA algorithms
 447 and executed the algorithms over three layers of synthetic MT data. One of which is expanded,
 448 and the other is contracted by 10 % of the initial search range. We infer from three layers of
 449 synthetic data, results fluctuate by approximately 3 % from the true value when the search range



450 is changed. This variation is about 10 % on average for synthetic data corrupted with 30 % random
 451 noise, as shown in Table 2.

452 **Table 2** Stability analysis of a hybrid algorithm for three layers of synthetic data.

Layer parameters		ρ_1 (Ωm)	ρ_2 (Ωm)	ρ_3 (Ωm)	h_1 (m)	h_2 (m)
Search Range		5000- 50000	1000- 10000	50-5000	5000- 25000	10000- 25000
Search Range - Case 1		4500- 55000	900- 11000	45-5500	4500- 27500	9000- 27500
wPSOGSA inverted model	0 %	31092.47	5085.79	1000.14	14700.83	18251.85
	30 %	30113.82	5016.75	1137.05	15880.95	23970.22
Search Range - Case 2		5500- 45000	1100- 9000	55-4500	5500- 22500	11000- 22500
wPSOGSA inverted model	0 %	29078.26	4922.85	999.91	15273.25	17767.45
	30 %	27815.97	5464.88	1156.46	17398.41	18119.61

453

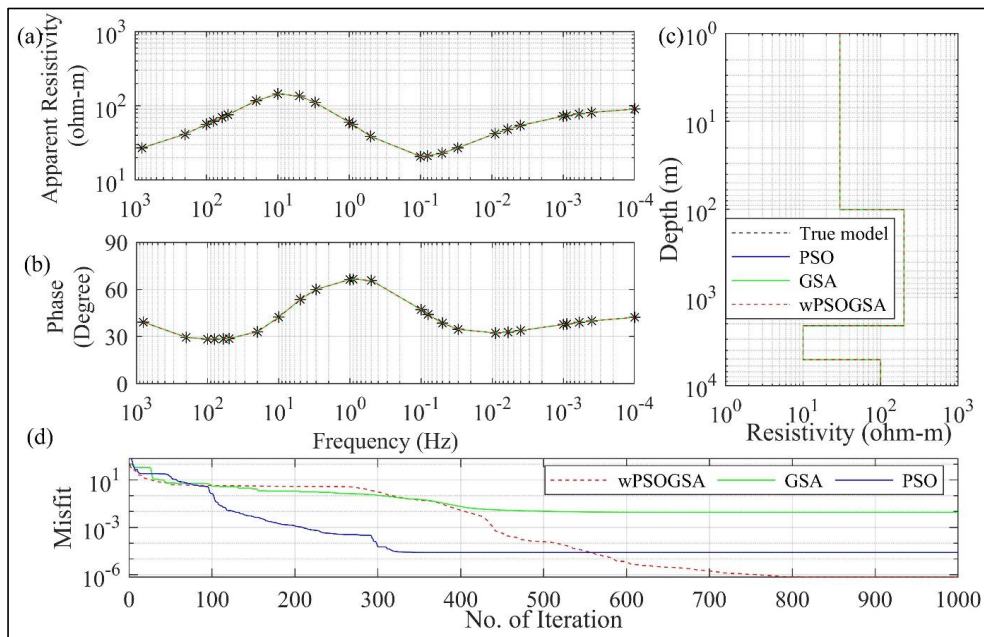
454 **4.2 Application to synthetic MT data-Four layers case**

455 For the second example of the synthetic data, a typical four-layer HK-type of earth model taken
 456 from Xiong et al. (2018) is generated by forward modeling equations for demonstration of the
 457 wPSOGSA, PSO, and GSA algorithms and compared their performance with Improved
 458 Differential Evolution (IDE) results obtained by Xiong et al. (2018). Analysis over noisy synthetic
 459 data is done by corrupting synthetic data with 10 % and 20 % Gaussian random noise to mimic
 460 the real field data because different types of noises influence apparent resistivity data. Following
 461 that, all three optimization methods are run using the noisy synthetic data. As the misfit error
 462 increases with the noise in the data, the Bayesian PDF of 68.27 % CI is calculated with respect to
 463 the threshold misfit error of 0.01 and thus the mean model is calculated.

464 Enormous uncertainty is shown in the inverted results; hence, we calculated the mean
 465 model for 68.27 % CI using posterior Bayesian PDF to reduce the uncertainty and produce the



466 global best solution. The optimized results obtained from the posterior PDF and the true model
 467 are shown in Table 3. Fig. 11 illustrate the inverted responses for PSO, GSA, and wPSOGSA are
 468 well-fitting as follows (a) observed and calculated apparent resistivity data, (b) observed and
 469 calculated apparent phase data, (c) 1-D depth model, and (d) convergence response of present
 470 algorithms. We have estimated the layer parameters for synthetic data corrupted with 20 % random
 471 noise for comparative analysis and found that the PSO, GSA, and wPSOGSA converge at
 472 iterations 96, 556, and 187 with associated errors 3.69, 4.04, and 3.69, respectively.



473
 474 **Figure 11** The inverted MT response by PSO (blue color), GSA (green color), and hybrid
 475 wPSOGSA (red color) with a true model (black color) over four-layer synthetic data as shown in
 476 (a) observed and calculated apparent resistivity curve, (b) observed and calculated apparent phase
 477 curve, (c) 1D depth inverted model and (d) convergence curve

478 Additionally, the synthetic data corrupted with 10 % random noise is also used and
 479 executed inversion, keeping the search range, a number of particles, and iterations the same as
 480 before and observed that the PSO, GSA, and wPSOGSA converge at iterations 151, 2 and 250



481 with associated error 1.7609, 1.95 and 1.76 respectively. The posterior Bayesian PDF for threshold
 482 data with 68.27 % CI is calculated similarly as a three-layer case to minimize the uncertainty in
 483 inverted results.

484

485 **Table 3** Comparison of the result obtained from improved Differential Evolution (IDE) and
 486 inverted results of PSO, GSA, and hybrid wPSOGSA obtained by using posterior PDF for four-
 487 layer synthetic apparent resistivity data with different Gauss noise levels (0 %, 10 %, and 20 %)
 488 and True model.

Layer parameters		ρ_1 (Ωm)	ρ_2 (Ωm)	ρ_3 (Ωm)	ρ_4 (Ωm)	h_1 (m)	h_2 (m)	h_3 (m)
True model		30.00	200.00	10.00	100.00	100.00	2000.00	3000.00
Search Range		25-35	100-250	5-15	50-150	50-200	1000-3000	2000-3500
0 % noise	IDE	30.00	200.00	9.99	100.01	100.00	1991.98	3000.24
	PSO	30.00	200.001	10.00	100.00	100.00	2000.00	3000.00
	GSA	29.95	199.79	9.99	99.99	99.67	2000.70	2995.37
	wPSOGSA	30.00	200.00	10.00	100.00	100.00	2000.00	3000.00
10 % noise	IDE	30.24	210.28	08.92	99.67	109.83	1994.63	2667.13
	PSO	32.86	224.99	11.51	107.65	109.71	1971.78	3499.92
	GSA	29.77	209.78	9.50	106.78	92.38	2073.14	2754.77
	wPSOGSA	30.46	197.18	9.97	102.01	100.50	1974.83	3079.35
20 % noise	IDE	30.30	212.41	11.44	97.92	102.40	1930.17	3347.24
	PSO	34.99	247.04	11.80	114.56	115.16	1986.08	3499.99
	GSA	29.52	225.61	9.74	113.46	87.55	2081.26	2753.29
	wPSOGSA	34.88	246.08	11.75	114.54	114.58	1990.98	3489.10

489

490



491 **4.2.1 Stability analysis**

492 For the stability evaluation of presented algorithms over four layers of synthetic MT data, similar
 493 to the three-layer case, we used two different search ranges and executed the algorithms for 1000
 494 iterations. The method exhibits good results with four layers of synthetic data and reveals minimal
 495 variation for noise-free data. For 30 % contaminated data, the variation is approximately 10 % and
 496 12 % in case 1 and case 2, respectively. The outputs don't change much across runs and provide
 497 consistent results, as shown in Table 4.

498

499 **Table 4** Stability analysis of a hybrid algorithm for four layers of MT synthetic data.

Layer parameters		ρ_1 (Ωm)	ρ_2 (Ωm)	ρ_3 (Ωm)	ρ_4 (Ωm)	h_1 (m)	h_2 (m)	h_3 (m)
Search Range		25-35	100-250	5-15	50-150	50-200	1000-3000	2000-35000
Search Range-Case 1		27.50-31.50	110-225	5.50-13.50	55-135	55-180	1100-2700	2200-3150
wPSOGSA	0 %	29.99	199.99	10.00	99.99	99.99	1999.99	3000.00
inverted model	30 %	31.5	220.79	11.17	109.18	99.48	2150.07	3150
Search Range-Case 2		22.50-38.50	90-275	4.50-16.50	45-165	45-220	900-3300	1800-3850
wPSOGSA	0 %	29.99	199.99	10.00	99.99	99.99	1999.99	3000.00
inverted model	30 %	35.47	264.27	11.95	103.13	116.22	2020.37	3040.95

500

501 **4.3 Application to field MT data-Island of Milos, Greece**

502 We utilized the first example of field data from the Island of Milos, Greece. Milos is a part of the
 503 South Aegean Active Volcanic Arc, an example of an emergent volcanic edifice (Stewart and
 504 McPhie, 2006) formed by monogenetic effusive and explosive magmatism pulses. Milos is the
 505 world's biggest exporter of bentonite, and it also has a diverse variety of metalliferous and non-
 506 metalliferous mineral reserves. It's a conserved on-land laboratory for studying shallow



507 underwater hydrothermal ore-forming processes. The accompanying shallow subsurface
508 hydrothermal venting fields have developed significantly less attention. ("Dawes, 1986) used
509 magnetotelluric data to assess the resistivity structure of the geothermal area on Milos west side.
510 With around 3.0 km spacing, 37 MT probes in the bandwidth of 100-0.01 Hz and 12 investigations
511 in the bandwidth of 0.01-0.0001 Hz were installed along with various profiles that were
512 perpendicular to the Zephyria graben in the W-E direction, as well as along the graben in S-N
513 direction (Hutton et al. 1989). The location of the MT site and the geology of the study area are
514 shown in Fig. 12.

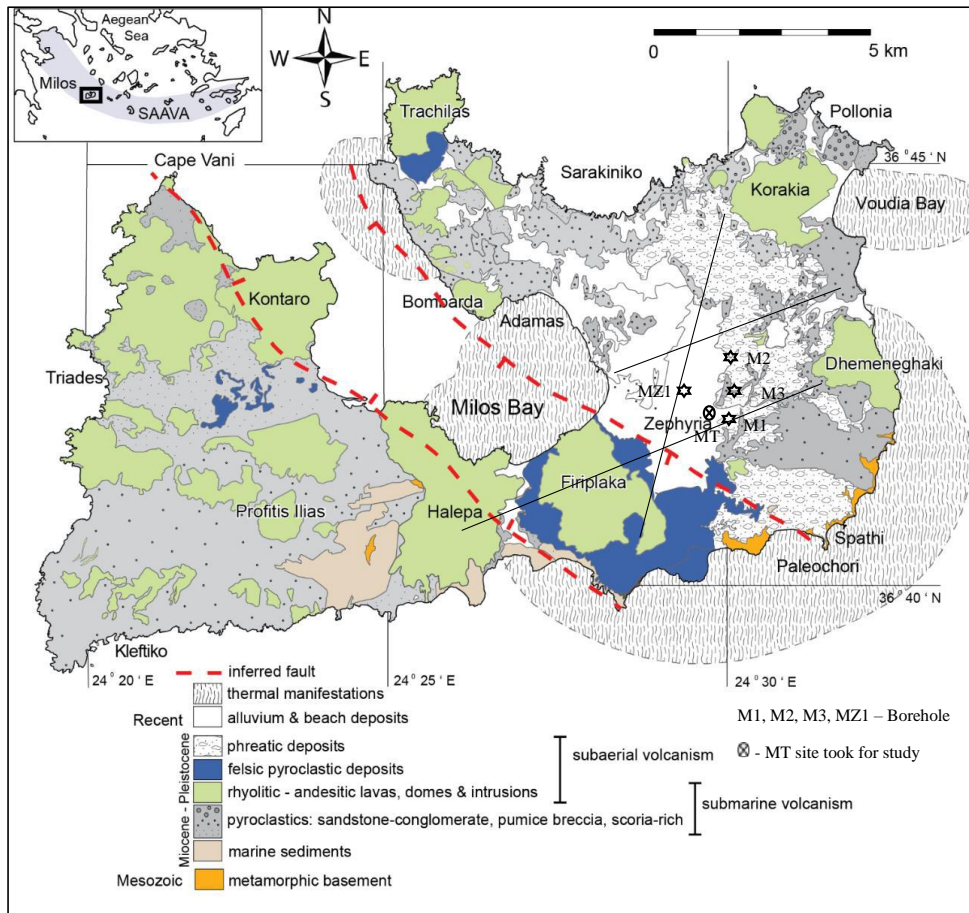
515 In one-dimensional MT data for site G5 near borehole M2 (Hutton et al., 1989) the
516 apparent resistivity and phase values are inverted using the wPSOGSA, PSO, and GSA, keeping
517 the same set of controlling parameters as for noisy synthetic data, such as the swarm size, inertia
518 weight (w), personal learning coefficient (c_1) and a global learning coefficient (c_2), descending
519 coefficient (α), and the initial value of universal gravitational constant (G_0).

520 Figure 13 shows the calculated data and model parameters as (a) match between observed
521 and computed apparent resistivity data, (b) match between observed and computed apparent phase
522 data, and (c) 1D inverted model and (d) convergence response of wPSOGSA (red color), GSA
523 (green color), and PSO (blue color) along with true model (black color). In subfigure Fig. 13(c)
524 depicts alluvium deposits with a resistivity of $1.0 \Omega\text{m}$ with 15 m thickness as the top layer, and
525 volcanic deposits with a resistivity of $300 \Omega\text{m}$ and 10 m thickness lie beneath the alluvium
526 deposits. A very high conducting layer of resistivity less than $1.0 \Omega\text{m}$ is estimated, equivalent to
527 the green lahar under the high resistivity volcanic deposits. The next layer below, with higher
528 resistivity, corresponds to the crystalline foundation. In the geothermal zone's depths, the
529 resistivity drops again. The resistivity in the depth range of about 1000 m, which is similar to
530 earlier studies, was explored, and the findings of the proposed algorithm discovered to be in good
531 agreement with model developed by Dawes in Hutton et al. (1989).

532

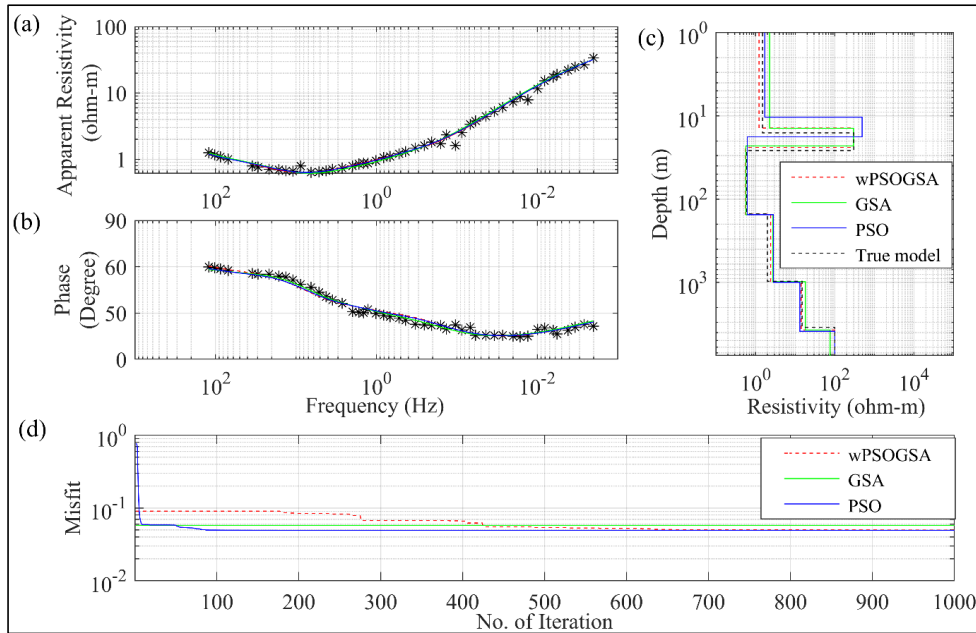


533



534 **Figure 12** The location of the MT site and geology of the Island of Milos, Greece (modified after
535 (Stewart and McPhie, 2006))

536 In subfigure Fig. 13(d) reveals that the algorithms converge at iterations 218, 1, and 425
537 with corresponding errors of 0.0494, 0.0518, and 0.0493 for PSO, GSA, and wPSOGSA,
538 respectively. The hybrid algorithm has the least error between observed and computed data. The
539 algorithms are executed for 1000 iterations and 10000 models, and findings are compared with
540 available stratigraphy, and the result is derived using the Monte-Carlo technique by Hutton et al.
541 (1989). After examining our optimized effects from Fig. 13 and Table 5, hybrid wPSOGSA
542 outperformed PSO and GSA.



543

544 **Figure 13** The inverted MT response by PSO (blue color), GSA (green color), and hybrid
 545 wPSOGSA (red color) with a true model (black color) over the geothermal area, Island of Milos,
 546 Greece, as shown in (a) observed and calculated apparent resistivity curve, (b) observed and
 547 calculated apparent phase curve, (c) 1D depth inverted model and (d) convergence curve

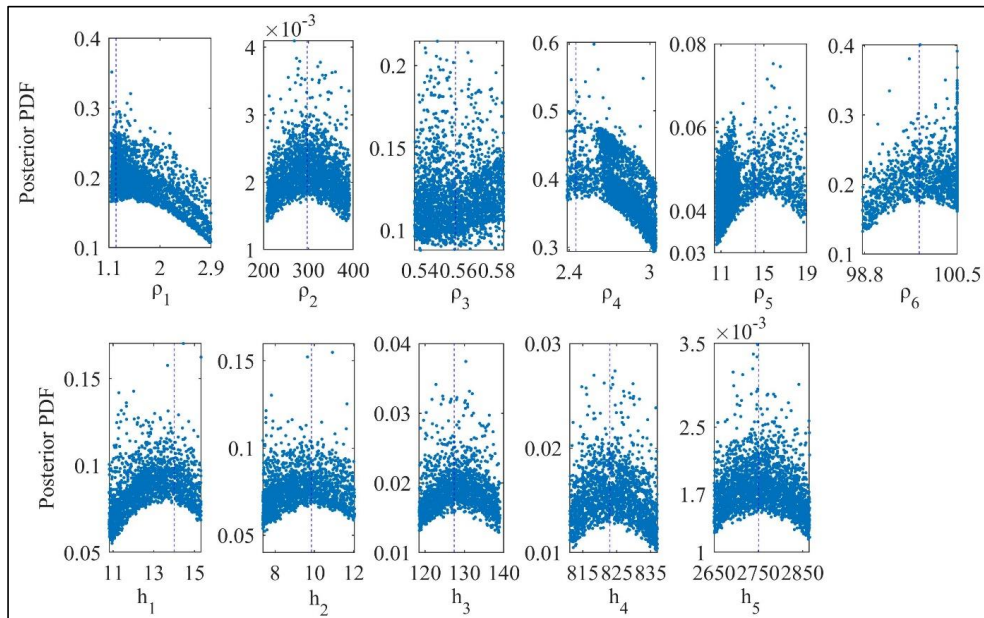
548

549 **4.3.1 Bayesian analysis and uncertainty in model parameters**

550 A posterior Bayesian method determines the global model and related uncertainty. Figure 14
 551 shows another uncertainty study that examined the six-layered resistivity model over the
 552 geothermal field, Island of Milos, Greece, and found that the peak values of the posterior PDF for
 553 all model parameters are very nearer to the actual value of the layer parameters, providing less
 554 uncertainty. We have analyzed the wPSOGSA inverted results from the Fig. 14 and Table 5 and
 555 found that the first, second, third, fourth, fifth, and sixth layers' resistivity with uncertainty in
 556 associated layer parameters is $1.23 \pm 0.49 \Omega\text{m}$, $297.61 \pm 53.43 \Omega\text{m}$, $0.55 \pm 0.02 \Omega\text{m}$, $2.41 \pm 0.16 \Omega\text{m}$,
 557 $14.18 \pm 1.76 \Omega\text{m}$, and $99.92 \pm 0.37 \Omega\text{m}$. Similarly, the associated thicknesses with uncertainty are



558 14.51±1.35 m, 9.85±1.35 m, 127.39±6.01 m, 823.01±7.57 m, and 2750.88±63.07 m. Thus, the
559 analysis suggests the lesser uncertainties in each layer's parameters except resistivity of the first
560 and second layers.



561

562 **Figure 14** Posterior Bayesian probability density function (PDF) with 68.27 % CI for
563 wPSOGSA over a geothermal field, Island of Milos, Greece

564

565 Table 5 compares optimized results obtained from all three presented algorithms based
566 on posterior Bayesian PDF under 68.27 % CI condition. However, the 1D depth model inverted
567 from wPSOGSA shows good agreement with the available borehole M-2 (Hutton et al., 1989).
568 As a result, the hybrid algorithm is functioning better, and the findings are encouraging.

569

570

571

572

573



574 **Table 5** Search range and inverted results by posterior PDF (68.27 % CI) and PSO, GSA, and
 575 hybrid wPSOGSA for six-layered field data.

Layer parameters		ρ_1	ρ_2	ρ_3	ρ_4	ρ_5	ρ_6	h_1	h_2	h_3	h_4	h_5
		(Ωm)	(Ωm)	(Ωm)	(Ωm)	(Ωm)	(Ωm)	(m)	(m)	(m)	(m)	(m)
Search Range		0.1- 5	50- 500	0.1- 5	1- 10	10- 30	50- 100	10- 20	5- 15	110- 150	800- 850	2500- 3000
Mean	PSO	1.71	493.81	0.62	2.82	13.22	99.97	10.39	7.44	135.4	843.77	2861.35
	GSA	2.28	299.28	0.54	2.76	18.25	76.03	14.08	8.81	130.75	825.32	2753.07
Posterior	wPSOGSA	1.23	297.61	0.55	2.41	14.18	99.92	14.51	9.85	127.39	823.01	2750.88

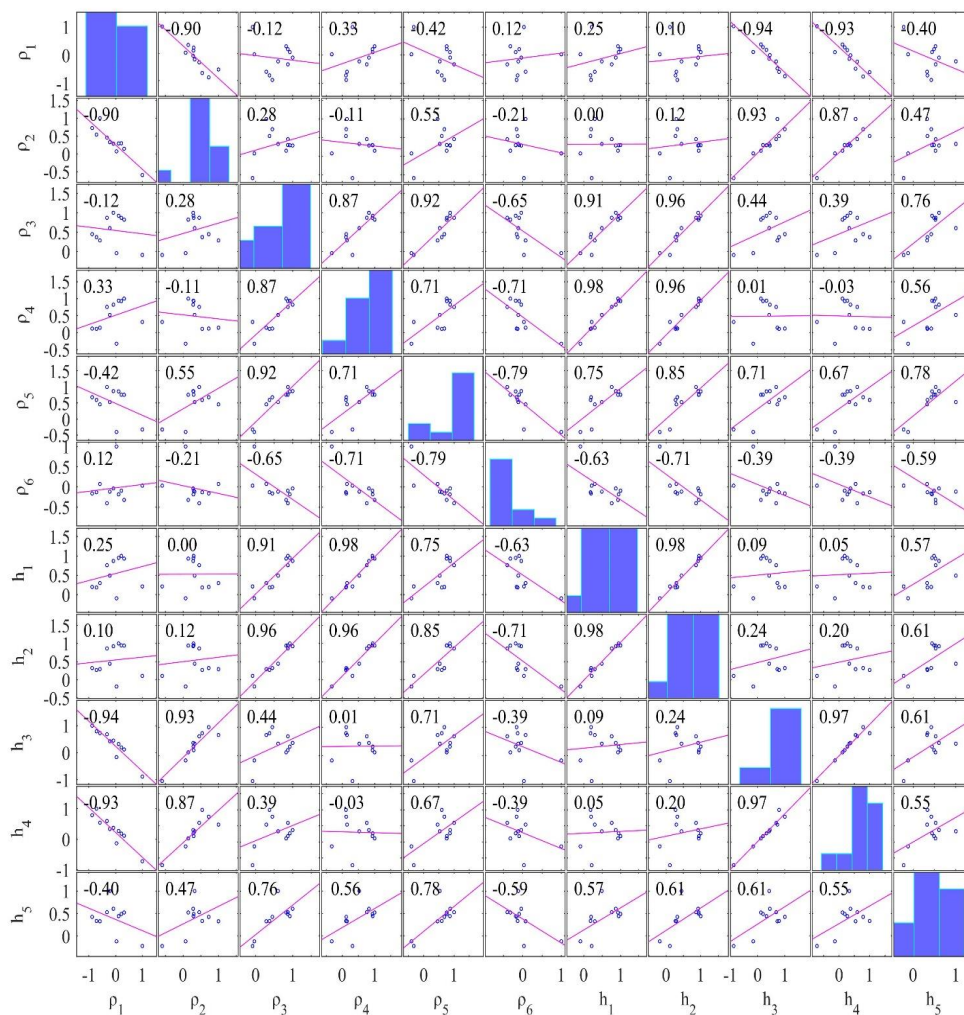
576

577 **4.3.2 Sensitivity, correlation matrix, and model parameters**

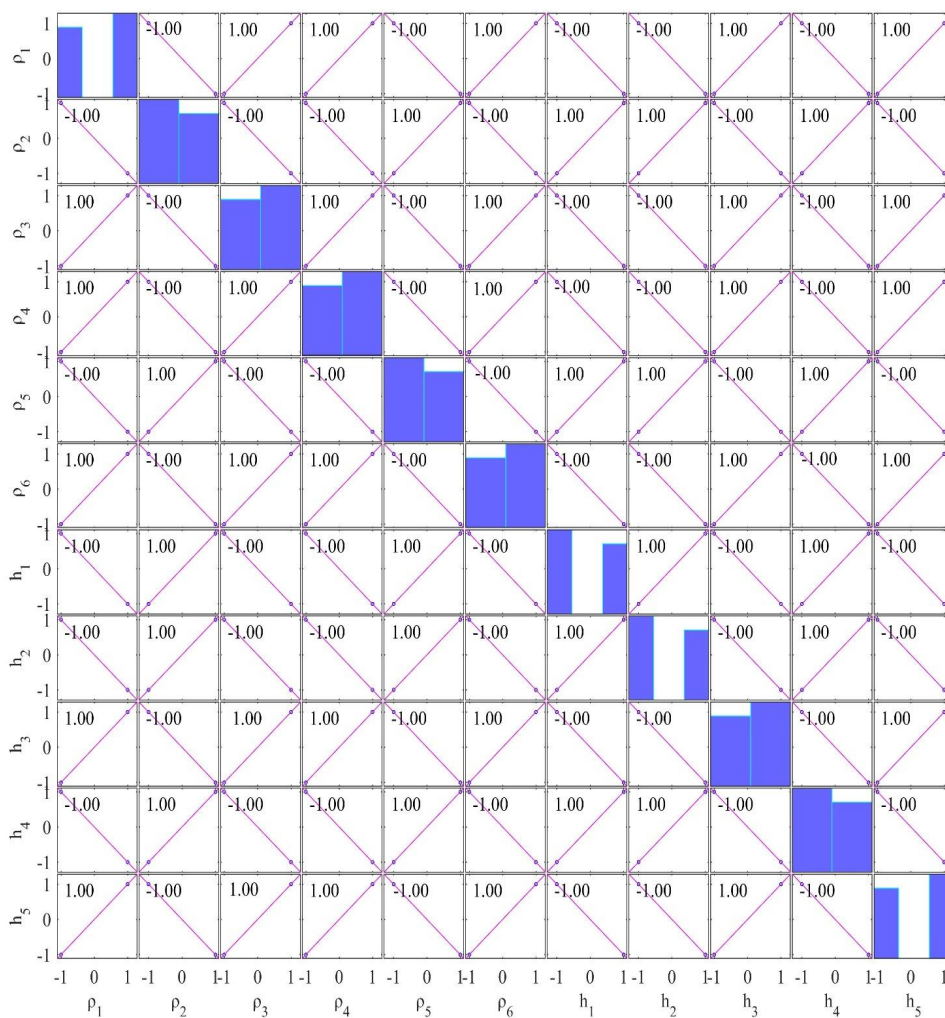
578 Here a similar study of the correlation matrix is carried out for field example from the Island of
 579 Milos, Greece using all accepted models, which have posterior PDF values within 68.27 % CI.
 580 The correlation matrix of PSO, GSA, and wPSOGSA was examined over the field MT data as
 581 shown in Fig. 15, Fig. 16 and Fig. 17 demonstrating the sensitivity among inverted model
 582 parameters and found an almost similar correlation among the layer parameters for three-layer
 583 synthetic study. From correlation analyses, we noticed that the values are showing moderate and
 584 weak correlation among parameters in the wPSOGSA case, indicating that wPSOGSA is linearly
 585 independent of layer parameters, while PSO and GSA are more reliant, so changing one parameter
 586 will show less effect on the other. This indicates that the parameter is less affected by other layer
 587 parameters and resistivity curves. Whereas the correlation among layer parameters for field data
 588 using GSA is either strongly positive or strongly negative, which describes that the parameters are



589 dependent on each other. Thus a change in one parameter affects the other, and also apparent
 590 resistivity curve is very much involved.



591 **Figure 15** Correlation matrix of field data taken from the geothermal rich area, Island of Milos,
 592 Greece for PSO

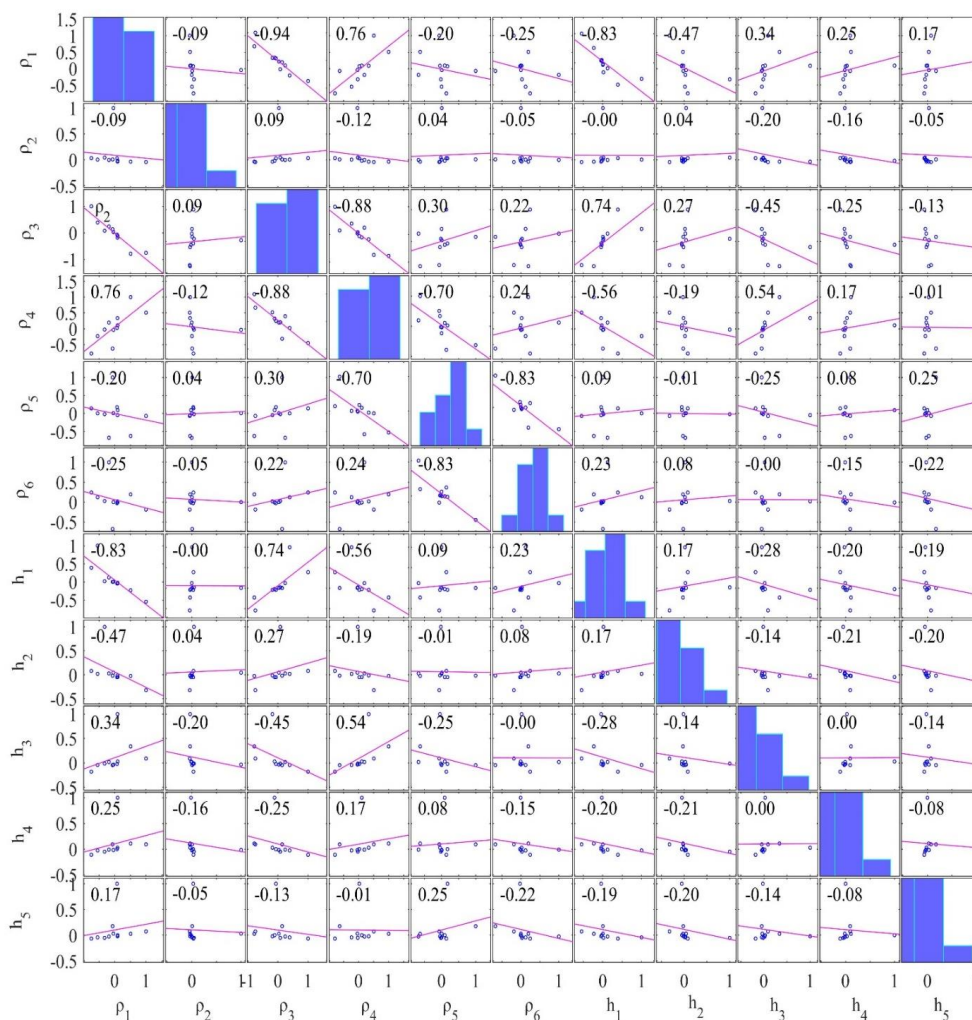


593 **Figure 16** Correlation matrix of field data taken from island geothermal rich area of Milos, Greece

594 for GSA

595

596



597 **Figure 17** Correlation matrix of field data taken from island geothermal rich area of Milos, Greece
 598 for hybrid wPSOGSA

599

600 **4.4 Application to field MT data-Newcastleton, Southern upland, Scotland**

601 Another field example of MT data was picked to illustrate our technique from Newcastleton

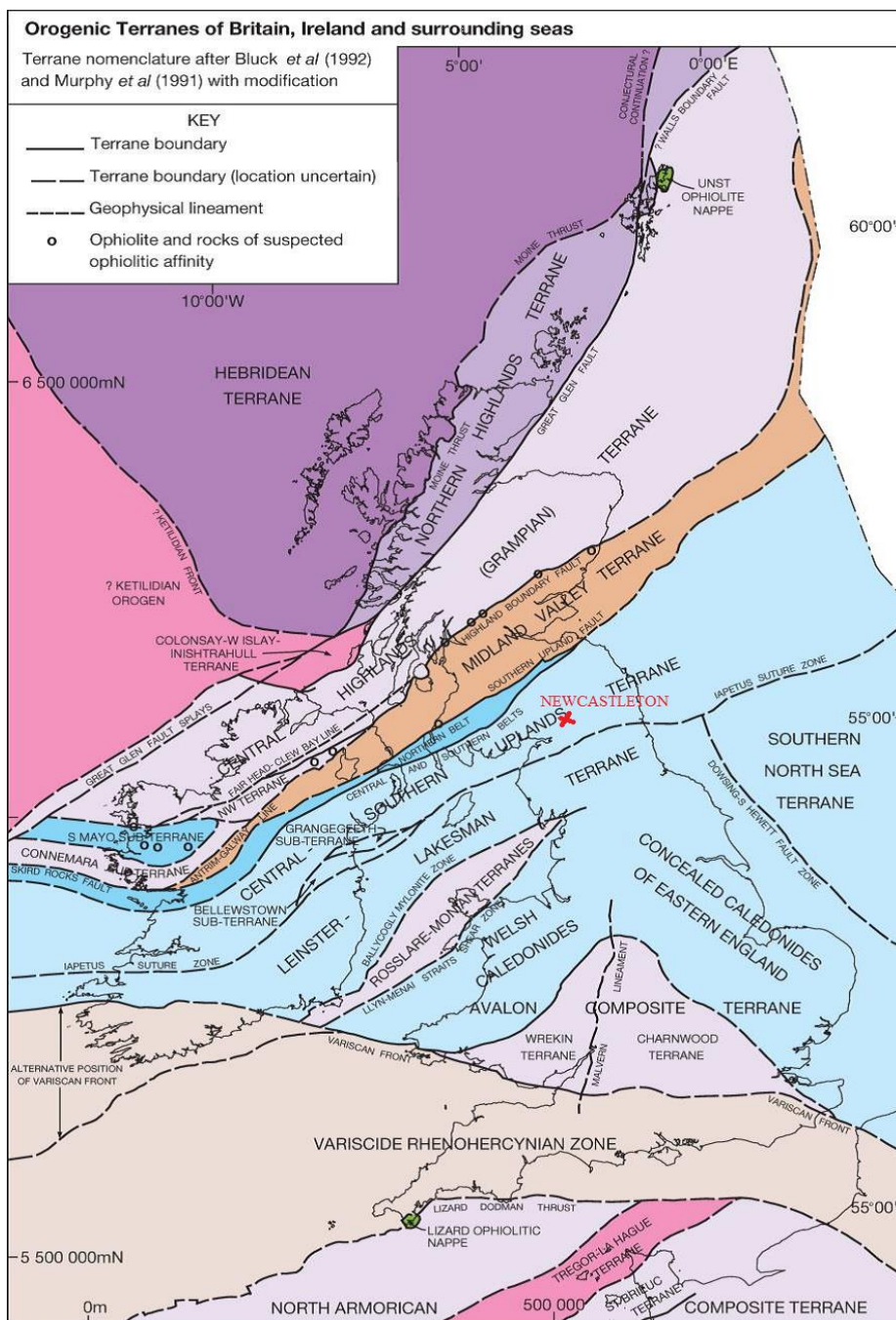
602 (2.796° W, 55.196° N in Geographic coordinates), Southern Uplands of Scotland. By the Southern



603 Uplands fault, the Southern Uplands are isolated from the Midland Valley. The bulk of the
604 Southern Uplands comprises Silurian/Lower Paleozoic sedimentary deposits such as greywackes
605 and shales that originated in the Iapetus Ocean during the late Neoproterozoic and early Paleozoic
606 geologic eras. These rocks emerged from the seafloor as an accretionary wedge during the
607 Caledonian orogeny. The majority of the rocks are coarse greywacke, a kind of sandstone that has
608 been poorly metamorphosed and contains angular quartz, feldspar, and small rock fragments. The
609 Midland Valley and Northern England, on the other hand, are known for their thick Carboniferous
610 layers, which are used to measure coal. The geomagnetic studies by Jones and Hutton (1979) have
611 shown that the Southern Uplands are characteristic of a typical continent, with a zone of very high
612 electrical conductivity. The location of the MT site and the geology of the study area are shown
613 in Fig. 18.

614 During nine days in the frequency range of 0.1 Hz to 0.0001 Hz, the variations of the
615 magnetic and telluric fields concerning the time at four sites along a line perpendicular to the
616 anomaly's strike were recorded, keeping a high signal to noise ratio where the anisotropy ratios
617 are so near to one and the skew factor is less than 0.1 for the majority of periods. Due to low
618 anisotropy ratios and skew factor, the resistivity distribution under this location is one-dimensional
619 (Jones and Hutton, 1979). Here one set of MT data is inverted using PSO, GSA, and wPSOGSA
620 to obtain the best fitting apparent resistivity curve, apparent phase curve, and 1D depth model as
621 shown in subfigures Fig. 19(a), Fig. 19(b), and Fig. 19(c), respectively. Figure 19 shows a realistic
622 one-dimensional resistivity variation, with a phase response ranging from 60° at 100 seconds to
623 35° at 1000 seconds, which can only be obtained by establishing a conducting zone at lower
624 crustal/upper mantle levels (Jones and Hutton, 1979).

625 The execution time for wPSOGSA (33 seconds) is the least as compared to GSA (34
626 seconds) and PSO (53 seconds). The convergence iterations are 79, 101, and 65, and associated
627 misfit errors are 3.79, 4.72, and 3.70 for PSO, GSA, and wPSOGSA, respectively.



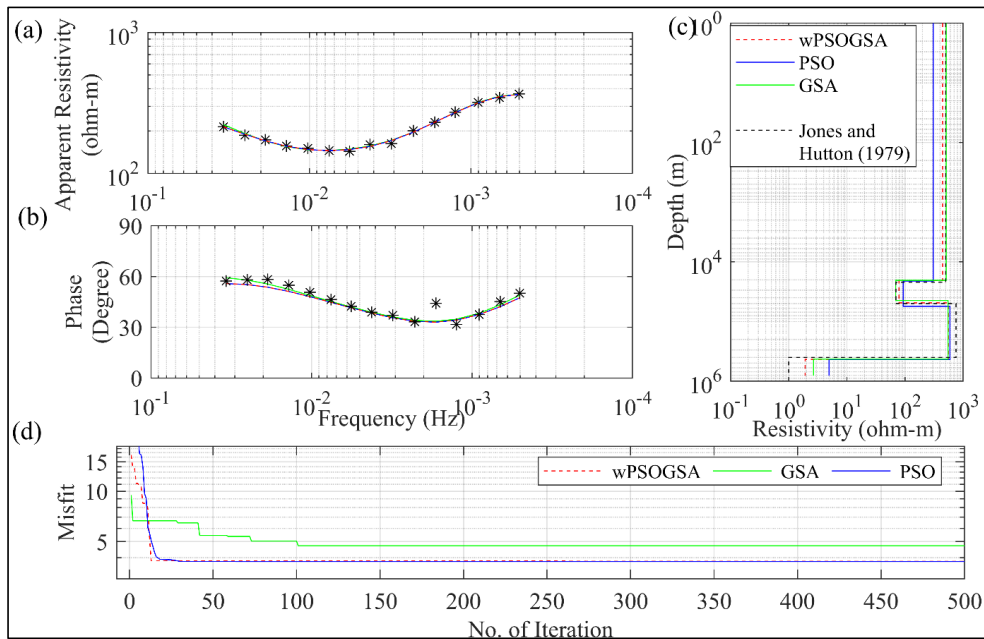
628

629 **Figure 18** The location of MT site and geology of the Southern upland, Scotland (after BGS,

630 2016)



631 The inverted MT model is illustrated in subfigure Fig. 19(c), which depicts two low
632 conductive zones at a depth of 21 km and 400 km. The first conductive layer ($70 \Omega\text{m}$) with a
633 thickness of 28 km is underlain by a high resistive top layer of thickness of 21 km, and the second
634 very high conductive layer (less than $1.0 \Omega\text{m}$) at a depth of 400 km is underlain by high resistive
635 layer ($550 \Omega\text{m}$) of thickness 351 km. Thus the last layer of a very high conductive zone (i.e.,
636 resistivity less than $1.0 \Omega\text{m}$) as a lower crust/upper mantle conductor at a depth of 400 km is
637 estimated. At 400 m depths, a conducting zone meets both the amplitude and phase long period
638 responses. This explanation is directly equivalent to accepted models derived from Monte-Carlo
639 models for the structure underlying the Southern Uplands.



640
641 **Figure 19** The inverted MT response by PSO (blue color), GSA (green color), and hybrid
642 wPSOGSA (red color) with a true model (black color) over Newcastleton, Southern Scotland, as
643 shown in (a) observed and calculated apparent resistivity curve, (b) observed and calculated
644 apparent phase curve, (c) 1D depth inverted model and (d) convergence curve
645



646 **Table 6** Search range, inverted results by posterior PDF (68.27 % CI) using PSO, GSA, and
 647 wPSOGSA for field data.

Layer parameters	ρ_1 (Ωm)	ρ_2 (Ωm)	ρ_3 (Ωm)	ρ_4 (Ωm)	h_1 (m)	h_2 (m)	h_3 (m)
Search Range	300-1000	10-150	250-1500	0.1-5	10000-30000	15000-35000	100000-450000
Mean	304.47	92.66	591.52	4.93	20894.01	34776.15	379563.48
Posterior	507.65	69.38	548.46	2.66	20493.18	24182.99	382090.23
	444.27	78.94	554.53	1.91	20591.39	28177.40	382181.50

648

649 **5 Conclusions**

650 The study presented the wPSOGSA algorithm along with PSO and GSA to evaluate their efficacy
 651 and applicability to the MT data, which narrates the appraisal of 1D resistivity models from
 652 apparent resistivity, apparent phase, and the frequency data sets. So, synthetic and field MT data
 653 from various geological terrains were used to demonstrate the relevance of these methods, which
 654 are further carried out by applying multiple runs, generating a large number of models that fit the
 655 apparent resistivity and apparent phase curves. Then these best-fitting models within a specified
 656 range are then chosen for statistical analysis. The statistical analysis includes posterior PDF based
 657 on the Bayesian approach with 68.27 % CI, correlation matrix, and stability analysis to enhance
 658 the accuracy of the mean model with the least uncertainty. However, a solution from the posterior
 659 PDF based on the Bayesian of wPSOGSA is better than GSA, and PSO yields the reliability of the
 660 inversion algorithm. In general, conventional techniques can effectively resolve the model in
 661 random noise, but they can miscarry in methodical error or inappropriate models. The performance
 662 of the proposed algorithms has been analyzed based on the mean model, uncertainty, and stability
 663 of layered earth models, and found that the results obtained from wPSOGSA are reliable, stable,
 664 and more accurate than the available results, which are fitted well with borehole lithology.

665



666 **Acknowledgments**

667 The authors would like to express their gratitude to the IIT(ISM), Dhanbad, for providing a
668 pleasant environment to pursue this study and support for the research. We also express our
669 gratitude to the Editor-in-Chief, Associate Editor, and anonymous reviewers, whose suggestions
670 and comments enabled us to better understanding of the issue and considerably improve our
671 manuscript.

672

673 **Declarations**

674 **Competing interests**

675 The authors have no relevant financial or non-financial interests to disclose and no competing
676 interests to declare that are relevant to the content of this article. All authors certify that they have
677 no affiliations with or involvement in any organization or entity with any financial interest or non-
678 financial interest in the subject matter or materials discussed in this manuscript.

679

680 **Data availability statement**

681 The datasets used for the present study and analysis have been taken from published paper, cited
682 in the manuscript.

683

684 **Authors' contribution statement**

685 **Mukesh:** Conceptualization of the study, Methodology, Computer code, Analysis, Drafting of
686 the manuscript.

687 **Kuldeep Sarkar:** Methodology, Computer code, Analysis, Drafting the manuscript

688 **Upendra K. Singh:** Supervision, Suggestions, and editing.

689

690

691



692 **References**

- 693 Cagniard, L.: Basic theory of the magneto-telluric method of geophysical prospecting, *Geophys*,
694 18, 605–635, <https://doi.org/10.1190/1.1437915>, 1953.
- 695 Colorni, A., Dorigo, M., and Maniezzo, V.: Distributed Optimization by Ant Colonies,
696 Proceedings of the First European Conference on Artificial Life, Paris, France, 134–142 pp.,
697 1991.
- 698 Constable, S. C., Parker, R. L., and Constable, C. G.: Occam's inversion: A practical algorithm
699 for generating smooth models from electromagnetic sounding data, *Geophys*, 52, 289–300,
700 <https://doi.org/10.1190/1.1442303>, 1987.
- 701 "Dawes, G. J. K. ": Magnetotelluric feasibility study: Island of Milos, Greece, Luxembourg,
702 1986.
- 703 Dosso, S. E. and Oldenburg, D. W.: Magnetotelluric appraisal using simulated annealing,
704 *Geophys. J. Int.*, 106, 379–385, <https://doi.org/10.1111/j.1365-246X.1991.tb03899.x>, 1991.
- 705 Hutton, V. R. S., Galanopoulos, D., Dawes, G. J. K., and Pickup, G. E.: A high resolution
706 magnetotelluric survey of the Milos geothermal prospect, *Geothermics*, 18, 521–532,
707 [https://doi.org/10.1016/0375-6505\(89\)90054-0](https://doi.org/10.1016/0375-6505(89)90054-0), 1989.
- 708 Jones, A. G. and Hutton, R.: A multi-station magnetotelluric study in southern Scotland – I.
709 Fieldwork, data analysis and results, *Geophys. J. Int.*, 56, 329–349,
710 <https://doi.org/10.1111/j.1365-246X.1979.tb00168.x>, 1979.
- 711 Kennedy, J. and Eberhart, R.: Particle swarm optimization, in: Proceedings of ICNN'95 -
712 International Conference on Neural Networks, 1942–1948 vol.4,
713 <https://doi.org/10.1109/ICNN.1995.488968>, 1995.



- 714 Khishe, M. and Mosavi, M. R.: Chimp optimization algorithm, *Expert Syst. Appl.*, 149, 113338,
715 <https://doi.org/10.1016/j.eswa.2020.113338>, 2020.
- 716 Kirkpatrick, S., Gelatt C., D., and Vecchi M., P.: Optimization by Simulated Annealing, *Science*,
717 220, 671–680, <https://doi.org/10.1126/science.220.4598.671>, 1983.
- 718 Kunche, P., Sasi Bhushan Rao, G., Reddy, K. V. V. S., and Uma Maheswari, R.: A new
719 approach to dual channel speech enhancement based on hybrid PSO-GSA, *Int. J. Speech*
720 *Technol.*, 18, 45–56, <https://doi.org/10.1007/s10772-014-9245-5>, 2015.
- 721 Li, S.-Y., Wang, S.-M., Wang, P.-F., Su, X.-L., Zhang, X.-S., and Dong, Z.-H.: An improved
722 grey wolf optimizer algorithm for the inversion of geoelectrical data, *Acta Geophys.*, 66, 607–
723 621, <https://doi.org/10.1007/s11600-018-0148-8>, 2018.
- 724 Lynch, S. M.: Introduction to applied Bayesian statistics and estimation for social scientists,
725 Springer, New York, 2007.
- 726 Miecznik, J., Wojdyła, M., and Danek, T.: Application of nonlinear methods to inversion of 1D
727 magnetotelluric sounding data based on very fast simulated annealing, *Acta Geophys. Pol.*, Vol.
728 51, nr 3, 307–322, 2003.
- 729 Mirjalili, S. and Hashim, S. Z. M.: A new hybrid PSO-GSA algorithm for function optimization,
730 in: 2010 International Conference on Computer and Information Application, 374–377,
731 <https://doi.org/10.1109/ICCIA.2010.6141614>, 2010.
- 732 Mirjalili, S., Mirjalili, S. M., and Lewis, A.: Grey Wolf Optimizer, *Adv. Eng. Softw.*, 69, 46–61,
733 <https://doi.org/10.1016/j.advengsoft.2013.12.007>, 2014.



- 734 Nabighian, M. N. and Asten, M. W.: Metalliferous mining geophysics—State of the art in the
735 last decade of the 20th century and the beginning of the new millennium, *Geophysics*, 67, 964–
736 978, <https://doi.org/10.1190/1.1484538>, 2002.
- 737 Pérez-Flores, M. A. and Schultz, A.: Application of 2-D inversion with genetic algorithms to
738 magnetotelluric data from geothermal areas, *Earth Planets Space*, 54, 607–616,
739 <https://doi.org/10.1186/BF03353049>, 2002.
- 740 Rashedi, E., Nezamabadi-pour, H., and Saryazdi, S.: GSA: A Gravitational Search Algorithm,
741 *Inf. Sci.*, 179, 2232–2248, <https://doi.org/10.1016/j.ins.2009.03.004>, 2009.
- 742 Rodi, W. and Mackie, R. L.: Nonlinear conjugate gradients algorithm for 2-D magnetotelluric
743 inversion, *Geophysics*, 66, 174–187, <https://doi.org/10.1190/1.1444893>, 2001.
- 744 Ross, S.: *Probability and statistics for engineers and scientists*, Elsevier, New Delhi, 2009.
- 745 Roy, A. and Kumar, T. S.: Gravity inversion of 2D fault having variable density contrast using
746 particle swarm optimization, *Geophys. Prospect.*, 69, 1358–1374, <https://doi.org/10.1111/1365-2478.13094>, 2021.
- 748 Sen, M. K. and Stoffa, P. L.: Bayesian inference, Gibbs’s sampler and uncertainty
749 estimation in geophysical inversion1, *Geophys. Prospect.*, 44, 313–350,
750 <https://doi.org/10.1111/j.1365-2478.1996.tb00152.x>, 1996.
- 751 Sen, M. K. and Stoffa, P. L.: *Global Optimization Methods in Geophysical Inversion*,
752 Cambridge University Press, Cambridge, <https://doi.org/10.1017/CBO9780511997570>, 2013.
- 753 Şenel, F. A., Gökçe, F., Yüksel, A. S., and Yiğit, T.: A novel hybrid PSO–GWO algorithm for
754 optimization problems, *Eng. Comput.*, 35, 1359–1373, <https://doi.org/10.1007/s00366-018-0668-5>, 2019.



- 756 Sharma, S. P.: VFSARES—a very fast simulated annealing FORTRAN program for
757 interpretation of 1-D DC resistivity sounding data from various electrode arrays, *Comput.*
758 *Geosci.*, 42, 177–188, <https://doi.org/10.1016/j.cageo.2011.08.029>, 2012.
- 759 Shaw, R. and Srivastava, S.: Particle Swarm Optimization: A new tool to invert geophysical
760 data, *Geophysics*, 72, <https://doi.org/10.1190/1.2432481>, 2007.
- 761 Simon, D.: Biogeography-Based Optimization, *IEEE Trans. Evol. Comput.*, 12, 702–713,
762 <https://doi.org/10.1109/TEVC.2008.919004>, 2008.
- 763 Simpson, F. and Bahr, K.: *Practical Magnetotellurics*, Cambridge University Press, 2005.
- 764 Stewart, A. L. and McPhie, J.: Facies architecture and Late Pliocene – Pleistocene evolution of a
765 felsic volcanic island, Milos, Greece, *Bull. Volcanol.*, 68, 703–726,
766 <https://doi.org/10.1007/s00445-005-0045-2>, 2006.
- 767 Storn, R. and Price, K.: Differential Evolution – A Simple and Efficient Heuristic for global
768 Optimization over Continuous Spaces, *J. Glob. Optim.*, 11, 341–359,
769 <https://doi.org/10.1023/A:1008202821328>, 1997.
- 770 Tarantola, A.: Inverse Problem Theory and Methods for Model Parameter Estimation,
771 <https://doi.org/10.1137/1.9780898717921>, 2005.
- 772 Tarantola, A. and Valette, B.: Generalized nonlinear inverse problems solved using the least
773 squares criterion, *Rev. Geophys.*, 20, 219–232, <https://doi.org/10.1029/RG020i002p00219>,
774 1982.
- 775 Ward, S. H. and Hohmann, G. W.: 4. Electromagnetic Theory for Geophysical Applications, in:
776 *Electromagnetic Methods in Applied Geophysics: Volume 1, Theory*, Society of Exploration
777 Geophysicists, 130–311, <https://doi.org/10.1190/1.9781560802631.ch4>, 1988.



- 778 Wen, L., Cheng, J., Li, F., Zhao, J., Shi, Z., and Zhang, H.: Global optimization of controlled
779 source audio-frequency magnetotelluric data with an improved artificial bee colony algorithm, *J.*
780 *Appl. Geophys.*, 170, 103845, <https://doi.org/10.1016/j.jappgeo.2019.103845>, 2019.
- 781 Whitley, D.: A genetic algorithm tutorial, *Stat. Comput.*, 4, 65–85,
782 <https://doi.org/10.1007/BF00175354>, 1994.
- 783 Xiong, J., Liu, C., Chen, Y., and Zhang, S.: A non-linear geophysical inversion algorithm for the
784 mt data based on improved differential evolution, *Eng. Lett.*, 26, 161–170, 2018.
- 785 Yang, X.-S.: A New Metaheuristic Bat-Inspired Algorithm, in: *Nature Inspired Cooperative*
786 *Strategies for Optimization (NICSO 2010)*, edited by: González, J. R., Pelta, D. A., Cruz, C.,
787 Terrazas, G., and Krasnogor, N., Springer Berlin Heidelberg, Berlin, Heidelberg, 65–74,
788 https://doi.org/10.1007/978-3-642-12538-6_6, 2010a.
- 789 Yang, X.-S.: Firefly algorithm, stochastic test functions and design optimisation, *Int J Bio*
790 *Inspired Comput*, 2, 78–84, <https://doi.org/10.48550/arxiv.1003.1409>, 2010b.
- 791 Zhang, Z., Ding, S., and Jia, W.: A hybrid optimization algorithm based on cuckoo search and
792 differential evolution for solving constrained engineering problems, *Eng. Appl. Artif. Intell.*, 85,
793 254–268, <https://doi.org/10.1016/j.engappai.2019.06.017>, 2019.
- 794